

# Design, Development and Scaling Analysis of a Variable Stiffness Magnetic Torsion Spring

Regular Paper

Angelo Sudano<sup>1,\*</sup>, Dino Accoto<sup>1</sup>, Loredana Zollo<sup>1</sup> and Eugenio Guglielmelli<sup>1</sup>

<sup>1</sup> University Campus Bio-Medico Rome, Rome Italy

\* Corresponding author E-mail: a.sudano@unicampus.it

Received 27 Jun 2012; Accepted 16 Oct 2013

DOI: 10.5772/57300

© 2013 Sudano et al.; licensee InTech. This is an open access article distributed under the terms of the Creative Commons Attribution License (<http://creativecommons.org/licenses/by/3.0>), which permits unrestricted use, distribution, and reproduction in any medium, provided the original work is properly cited.

**Abstract** In this paper we report on the design, modeling, experimental testing and scaling analysis of a novel Magnetic Variable stiffness spring-Clutch (MAVERIC) device, which may be used as the elastic element of Variable Stiffness Actuators (VSAs). The device, comprising two co-axial diametrically magnetized hollow cylinders, has two degrees of freedom: a rotation of the two cylinders around the common axis and a relative translation along the same axis. For small rotations, the torque arising from the magnetic interaction of the two cylinders is almost linearly proportional to their relative rotation, as in mechanical torsion springs. In addition, the stiffness of the equivalent spring can be varied continuously from a maximum value down to exactly zero by changing the axial overlap of the two cylinders. In this way the proposed device can be used both as a clutch (i.e., perfectly compliant element) and as a variable stiffness torsion spring. A prototype, designed after magnetostatic FEM simulations, has been built and experimentally characterized. The developed MAVERIC has an experimentally determined maximum transmissible torque of 109.81 mNm, while the calculated maximum stiffness is 110.2 mNm rad<sup>-1</sup>. The amplitude of the torque-angle characteristic can be tuned linearly with a sensitivity of 12.63 mNm mm<sup>-1</sup> rad<sup>-1</sup>. Further

simulations have been computed parameterizing the geometry and the number of pole pairs of the magnets. The maximum torque density reached for one pole pair is  $47.21 \cdot 10^3 \text{ N m m}^{-3}$ , whereas for a fixed geometry similar to that of the developed prototype, the maximum torque is reached for seven pole pairs. Overall, compared to mechanical springs, MAVERIC has no fatigue or overloading issues. Compared to other magnetic couplers, torsion stiffness can be varied continuously from a maximum value down to exactly zero, when the device acts as a disengaged clutch, disconnecting the load from the actuator.

**Keywords** Variable Stiffness Joint, Magnetic Compliant Element, Magnetic Clutch

## 1. Introduction

Compliant transmissions, equipped with sensors providing a feedback on the output torque, are used in a number of robotic applications. Examples include robotic hands, where the elastic elements are used to perform a stable grasp [1–3], flying robots, in order to estimate the pitch torques generated by wings during flapping [4] and robotic snakes, for estimating ground

contact forces [5]. Furthermore elastic elements are key components of Series Elastic Actuators (SEAs) [6–9], Variable Stiffness Actuators (VSAs) [10–18] and, more generally, of Variable Impedance Actuators (VIAs) [19], where damping can also be adjusted by properly controlling the device. In this field, a seminal work is that of Fasse et al. [20], where an electromagnetic variable impedance actuator is demonstrated, capable of exerting a torque much higher than that of the prototype described in this paper.

SEAs, VSAs and VIAs are usually composed of one or more actuator (pneumatic, hydraulic, electric), possibly embedding gearboxes, compliant transmissions and sensors measuring the deformation of the elastic elements [21]. Elastic elements are also used in compliant joints [22–28] as they are particularly useful in terms of intrinsic safety, as in the case of wearable robotics, or to tune the dynamical properties of the robot, as needed to establish an effective interaction with the environment and the wearer [29]. Elastic elements also provide the mechanical structure with the capability to efficiently store and release mechanical energy. This feature is particularly useful for the generation of oscillatory movements. Moreover, the elastic energy stored in compliant elements can be quickly released for fast operations.

In the development of SEAs and VIAs, the often conflicting main design requirements are: compactness, lightness, backdrivability, compliance adjustability, maximum torque, torque resolution and bandwidth. Any design asks for an application-specific trade-off among such requirements. For instance, *compactness* and *lightness* are key requirements for ungrounded robots; *backdrivability* (either intrinsic or control-based) is important in assistive and rehabilitation robotics; *stiffness adjustability* is important whenever the efficiency must be optimized. *Torque resolution* and *large torque bandwidth* are also conflicting requirements, the former asking for highly compliant elastic elements to increase sensitivity, the latter asking for high stiffness to improve system response.

Several torsion springs have been proposed so far, including: linear compression springs arranged so as to produce torsion elasticity [15, 23, 24, 30]; leaf springs [13, 31]; flexible joints [22, 32–34]; custom-shaped compliant elements [7, 26, 27].

Moreover, remotely operated magnetic springs have been successfully used to operate wireless bioptic tools [35].

Magnetic couplers are a good replacement of their mechanical counterparts in a number of applications, thanks to such features as simple maintenance, high reliability, no need for lubricants, high efficiency, precise peak torque transmission, inherent overload protection, reduced drivetrain pulsations, tolerance to misalignments and low noise. Conversely, magnetic couplers are inherently characterized by a residual compliance. Nonetheless, this drawback can be managed [36] and in some applications (e.g., SEAs, VIAs) it could be beneficially exploited. Although a number of magnetic springs with constant [37–41] and variable [42] stiffness have been proposed, to the best of our knowledge no

*variable stiffness* magnetic spring, that can also be used as a clutch, has been proposed up to now.

This paper demonstrates a synchronous one DOF magnetic coupler with diametrically magnetized permanent magnets, working as a tunable compliant torsion element, with a maximum stiffness that can be varied linearly from zero up to a maximum value. When stiffness is set to zero, the coupling behaves as an open clutch (i.e., no torque transmission).

The paper is organized as follows. Section 2 presents the concept of the variable stiffness compliant element; characterization and data analysis of the developed prototype are described in Section 3; in Section 4 a scaling analysis is presented; Section 5 presents some example applications. Conclusions and future works are discussed in Section 6.

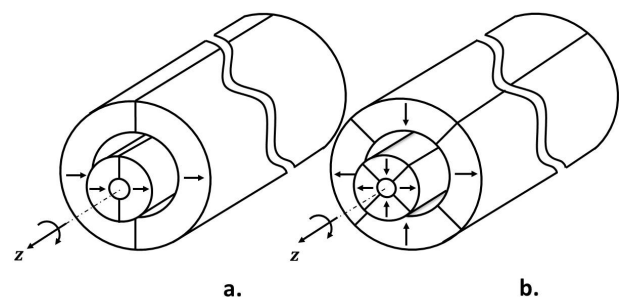


**Figure 1.** Permanent magnets configuration in MAVERIC: magnets are concentric and diametrically magnetized. They can rotate around and translate along the  $z$ -axis. a) One pole pair magnet configuration; b) two pole pairs magnet configuration.

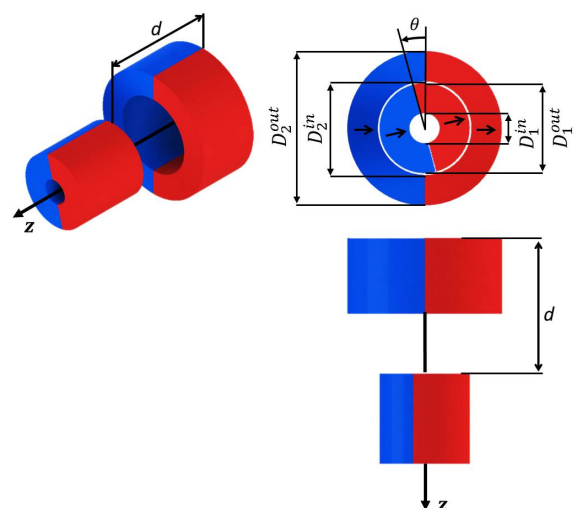


**Figure 2.** Configuration of permanent magnets selected for the setup.  $d$  and  $\theta$  respectively are the relative linear and angular displacement of magnets along  $z$  axis.  $D_1^{out}$ ,  $D_2^{out}$  are the inner and outer diameter of the outer magnet, while  $D_1^{in}$ ,  $D_2^{in}$  are the inner and outer diameters of the inner magnet.

## 2. The concept of a magnetic variable torsion stiffness compliant element

The proposed device, in the following referred to as Magnetic Variable stiffness spring-Clutch (MAVERIC), is a particular rotational magnetic coupler, comprising an inner and an outer part. The outer part consists of an even series of diametrically magnetized identical permanent magnets, placed in a cylindrical configuration, with alternate directions of magnetization. The concentric inner part has the same number of magnets, with alternate magnetization (Figure 1). The two nested magnetic cylinders are arranged in a two-DOF configuration, which allows the relative translation of the cylinders along the common axis and the rotation around the same axis. The axial displacement produces a change of the overlap of the two cylinders (Figure 2).

Keeping constant the magnetic properties of the permanent magnets, the stiffness can be varied by acting on the geometry of the device, e.g., by changing the thickness of the air gap between the inner and the outer parts or by varying their mutual overlap. The first solution is not only less practical from a design and fabrication point of view, but also less effective than the second one, as will be demonstrated below. Compared to the first one, the second option is not only simpler from a design point of view, but, more importantly, it allows reducing the stiffness of the coupler to zero, as needed for rendering a perfect compliance (clutch principle).

In order to demonstrate the working principle, let's consider a simple case of a rotary magnetic coupler with two nested concentric cylinders, both diametrically magnetized, so that each cylinder has one magnetic pole pair placed along the diameter (Figure 1-a). There are two main analytical approaches to derive the magnetic field from Maxwell's equations: the Coulombian and the Amperian current model [43]. Nevertheless, stiffness can be analytically calculated only in a limited number of simple cases while, in general, numerical methods are necessary. For the sake of analytically demonstrating the working principle, let's simplify the actual geometry by approximating the external magnetic cylinder (mean radius:  $r$ ) to a circle ( $M_{out}$  in Figure 4) and the inner cylinder to a magnetic dipole ( $M_{in}$  in Figure 4). Introducing a three-dimensional (3D) Cartesian coordinate system ( $x, y, z$ ) to represent this simplified configuration, assuming the magnetization vector of the external magnet to be constant and oriented along the  $x$  axis, it is practical to describe the magnetization of the external magnet as a magnetic moment per unit length:

$$\mathbf{m}_{out}^l = [m_{out}^l, 0, 0] \quad (1)$$

The magnetic moment of the inner part will have a constant module ( $m_{in}$ ) and a direction depending on the rotation angle ( $\theta$ ):

$$\mathbf{m}_{in} = m_{in} [\cos(\theta), \sin(\theta), 0] \quad (2)$$

The position of a generic magnet dipole in the external circle is:

$$\mathbf{r} = [r \cos(\theta_1), r \sin(\theta_1), z] \quad (3)$$

NdFeB magnets (HKCM engineering)		
Properties [unit]	Outer magnet	Inner magnet
Outer Diameter [mm]	$D_2^{out} = 20.6$	$D_1^{out} = 12$
Inner Diameter [mm]	$D_2^{in} = 12.5$	$D_1^{in} = 2$
Height [mm]	$h_2 = 10$	$h_1 = 12$
Max. Energy Product [BH <sub>max</sub> [kJ m <sup>-3</sup> ]	$394 \pm 12$	$410 \pm 12$
Coercive Force [kA m <sup>-1</sup> ]	796	796
Residual Induction [mT]	$1425 \pm 25$	$1455 \pm 25$

**Table 1.** Properties of the permanent magnets.

where  $z$  is the axial coordinate and  $\theta_1$  the angular position. The magnetic flux density, due to the external magnet, can be written as [44]:

$$\mathbf{B} = \frac{\mu_0}{4\pi} \int_0^{2\pi} \left( 3 \frac{(\mathbf{m}_{out}^l \mathbf{r}(\theta_1)) \mathbf{r}(\theta_1)}{|\mathbf{r}|^5} - \frac{\mathbf{m}_{out}^l}{|\mathbf{r}|^3} \right) r d\theta_1 \quad (4)$$

where  $\mu_0$  is the vacuum permeability. Substituting (1) and (3) in (4) it is possible to derive  $\mathbf{B}$ :

$$\mathbf{B} = \left[ \frac{\mu_0}{4} \frac{m_{out}^l r (r^2 - 2z^2)}{(r^2 + z^2)^{5/2}}, 0, 0 \right] \quad (5)$$

From (2) and (5) it is then possible to calculate the magnetic torque:

$$\boldsymbol{\tau} = \mathbf{m}_{in} \times \mathbf{B} = \left[ 0, 0, -\frac{m_{in} m_{out}^l \mu_0}{4} \frac{r \sin(\theta) (r^2 - 2z^2)}{(r^2 + z^2)^{5/2}} \right] \quad (6)$$

The torsion stiffness, function of  $\theta$ , is:

$$k(\theta) = \frac{d\tau_z(\theta)}{d\theta} = -\frac{m_{in} m_{out}^l \mu_0}{4} \frac{r \cos(\theta) (r^2 - 2z^2)}{(r^2 + z^2)^{5/2}} \quad (7)$$

where  $\tau_z(\theta)$  is the  $z$  component of  $\boldsymbol{\tau}$ . According to (7), keeping  $\theta$  constant, the maximum stiffness is reached for  $z = 0$ , while stiffness becomes zero when  $z = \pm r/\sqrt{2}$ . In the case where the control variable is  $r$  while  $z$  is constant, considering the conservation of magnetic dipoles numbers, i.e.,  $\frac{\partial}{\partial r} \left( \int_0^{2\pi} m_{out}^l r d\theta_1 \right) = 0$  (hence  $m_{out}^l = m_{out}/r$  where  $m_{out}$  is a constant), it can be inferred that the device could not be operated so to exhibit a stiffness ranging from zero up to its maximum: if  $z = 0$  stiffness cannot be zero, while, if  $z \neq 0$ , the maximum torque is the one obtained in correspondence to the minimum  $r$ .

Although the simple model described above can be useful in shedding some light on the working principle of MAVERIC, it is too simple to provide an accurate estimate of the expected performance of a real system. Conversely, magnetostatic equations are not amenable to being solved analytically given the complexity of the geometry. Therefore, FEM simulations have been performed with the purpose of dimensioning an experimental setup. Additional simulations have been used to compute the order of magnitude of the maximum reachable torque and the storable energy density.

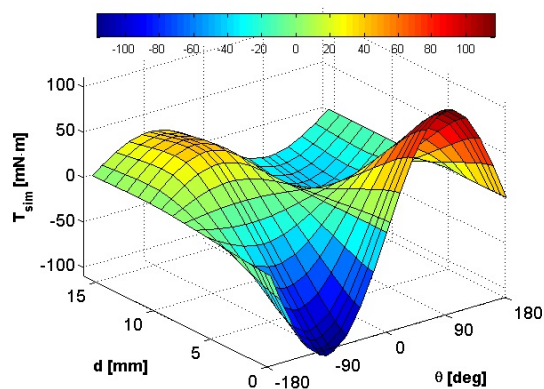


**Figure 3.** Torque simulation data in the function of magnet distance  $d$  and angle  $\theta$ . Maximum torque modulus is 116.54 mN·m, for  $d = 0$  mm and  $\theta = \pm 90^\circ$ , while  $d = d_0^{sim} = 7.12$  mm corresponds to perfect compliance condition.

### 3. Characterization

The MAVERIC system taken into account features one pole pair per cylinder (Figure 2). The characteristics of the selected magnets are reported in Table 1. In the following the torque is assumed positive if it tends to rotate the inner cylinder clockwise.

#### 3.1. Simulations

The magnet (NdFeB, HKCM engineering) dimensions and properties have been retrieved from the manufacturer's datasheet (Table 1). The selected rare-earth permanent magnets are characterized by a linear demagnetization curve and a high maximum energy product. Magnetostatic FEM simulations have been performed (Ansoft Maxwell 3D) taking into account a current free space. There are four main methods to numerically calculate forces/torques: the Maxwell stress tensor method, the co-energy method, the Lorentz force equation, and the rate of change of field energy method [45]. The selection of a specific method is usually problem-specific, although the most frequently used methods are the Maxwell stress tensor and co-energy methods. In our problem, where linear magnetic materials are considered, magnetic co-energy can be approximated to magnetic energy and forces/torques for different configurations can be calculated using the principle of virtual work. For the magnetostatic simulations, the linear and angular displacements  $d$  and  $\theta$  have been taken as parameters:  $d$  has been varied from 0 mm to 15.5 mm (steps of 0.5 mm for  $d \leq 1.5$  mm; steps of 1 mm for  $d > 1.5$  mm), while  $\theta$  has been varied from  $0^\circ$  to  $180^\circ$  (steps of  $20^\circ$ ; in addition,  $\theta = 90^\circ$  has been simulated, since this angular position corresponds to the maximum torque). Figure 3 shows how torque depends on those parameters. In the same figure it is possible to observe the sinusoidal profile related to angular displacement. Maximum torque modulus, retrieved from simulations, is 116.54 mN·m, for  $d = 0$  mm and  $\theta = \pm 90^\circ$ , whereas perfect compliance is achieved when  $d = d_0^{sim} = 7.12$  mm, as results from a linear interpolation.

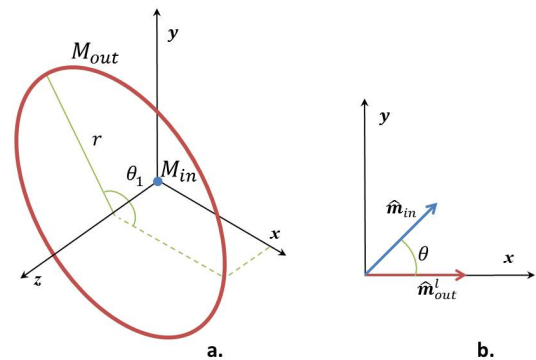


**Figure 4.** a) Simplified geometry of a rotary magnetic coupler with two nested concentric cylinders, both diametrically magnetized. The external magnetic cylinder (mean radius:  $r$ ) is approximated to the circle  $M_{out}$  (i.e., infinitesimal thickness and height), while the inner cylinder to the magnetic dipole  $M_{in}$ .  $\theta_1$  is the angular position of a generic magnetic dipole in the circle; b) orientations of  $\mathbf{m}_{out}^l$  and  $\mathbf{m}_{in}(\theta)$ .

#### 3.2. Experiments

In order to assess the reliability of the performed simulations, an actual prototype of MAVERIC has been built, using the same materials and geometric dimensions as in the simulation. The developed prototype has been experimentally characterized, as reported below.

##### 3.2.1. Setup

A custom measurement setup (Figure 5) has been assembled to measure torques in different configurations with a resolution of 1.0 mN·m. The setup comprises a linear and an angular micropositioner. The spring-loaded linear positioner allows a maximum displacement of 25.4 mm, with a  $1 \mu\text{m}$  resolution using the vernier scale (M-460P-X, Newport). The other positioner is a rotation stage that allows  $360^\circ$  of coarse and  $5^\circ$  of fine angular positioning: scale markings indicating every degree and vernier reading allow 5 arcmin positioning accuracy (M-481-A, Newport). Magnets have been connected to 3D-printed acrylic resin supports by means of shape coupling: a support, fixed to the rotating stage, houses the inner cylinder; the other cylinder is mounted on a shaft, supported by two ball bearings locked by two circlips in an A-shaped support, connected to the linear slide. An Al bar is fixed to the other end of the shaft. The head of a set screw in the bar localizes the contact point between the bar and the plate of a load cell (A120EC, Exacta; precision of  $1 \mu\text{N}$  and a range of 1.5 N). The torque exerted by MAVERIC is calculated by multiplying the lever arm of the bar and the force read by the load cell.

##### 3.2.2. Measurements

Exerted torques have been measured for 22 values of  $\theta$  in the interval  $[0^\circ, 360^\circ]$ , while  $d$  has been varied from 0 mm to 15.5 mm. Experimental data and their deviation from simulations are shown in Figure 6. In particular, the RMS error is 4.30 mN·m, i.e., less than 4% of the maximum measured torque (109.81 mN·m when  $d = 0$  mm and  $\theta = 90^\circ$ ). Perfect compliance is achieved when  $d = d_0^{exp} =$



6.78 mm. Torque-angle sinusoidal profile is confirmed by experimental data.

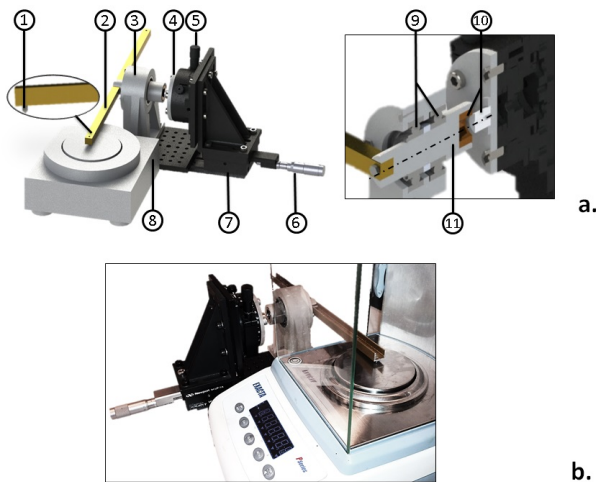


**Figure 5.** Overview of the experimental setup. a) CAD sketch: 1. set screw, 2. Al bar, 3. acrylic resin shaft A-shaped support, 4. rotation stage, 5. micrometer screw for angular displacements, 6. micrometer screw for linear displacements, 7. linear positioner, 8. load cell, 9. ball bearings, 10. permanent magnets, 11. acrylic resin shaft. b) Picture of the actual setup.

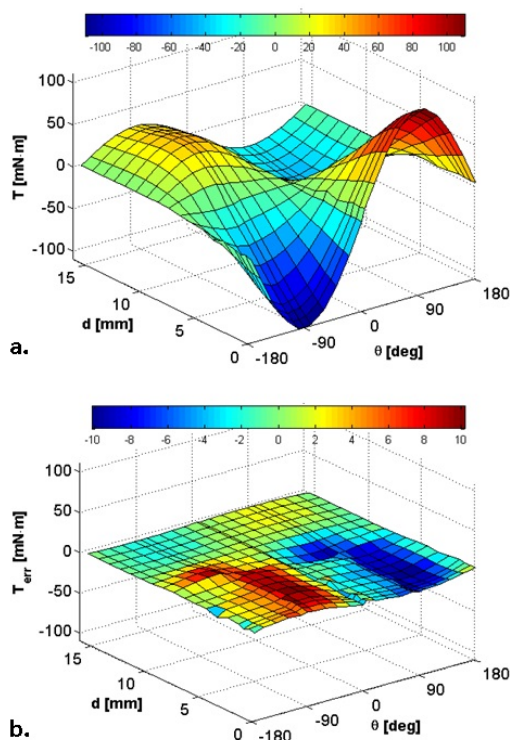


**Figure 6.** Torque data (experimental): a) Torque surface as a function of magnets distance  $d$  and rotation angle  $\theta$ . Maximum torque is 109.81 mN m, for  $d = 0$  mm and  $\theta = 90^\circ$ , while  $d = d_0^{exp} = 6.78$  mm corresponds to perfect compliance; b) Torque surface error calculated from simulation data ( $RMSE = 4.30$  mN m).

### 3.3. Torque fittings

The relation between maximum torque and magnet distance  $d$  in the configurations where there is overlap ( $0 \text{ mm} \leq d \leq 10 \text{ mm}$ ) is linear ( $R^2 = 0.994$ ), as reported in Figure 7. It is expected that the linearity of torque-angle characteristic is advantageous in SEAs and VIAs on the grounds that a linear elastic element simplifies the actuator model and the torque control. While the maximum torque-position relation is linear, the torque-angle characteristic is sinusoidal and its profile is preserved for any value of  $d$  (Figure 8). Torque-angle characteristic for  $d = 0$  mm can also be fitted as  $T = b_1 \sin(\theta)$  (Figure 9), with  $b_1 = 110.20$  mN m ( $R^2 = 0.999$ ,  $RMSE = 1.17$  mN m). It is also possible to linearly approximate the torque-angle characteristic in the range  $\pm 90^\circ$  (i.e.  $T = c_1 \theta$ ) obtaining  $R^2 = 0.920$  for a torsion stiffness  $c_1 = 79.41$  mN m rad $^{-1}$  ( $RMSE = 10.54$  mN m). A good analytical approximation of the torque function based on the experimental data is given by the following parametric surface (Figure 10):

$$T(\theta, d) = (A - Bd) \sin(\theta) \quad (8)$$

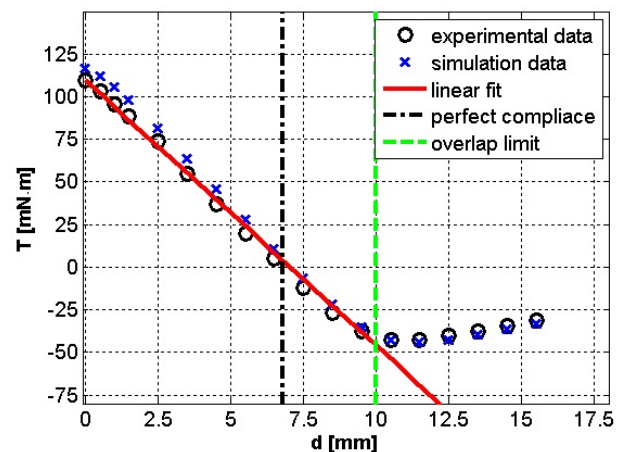


**Figure 7.** Maximum torque-magnet distance profile. Experimental data are fitted with  $T = a_1 - d a_2$  in the range of overlapping ( $d = 0 \text{ mm} \div 10 \text{ mm}$ ) resulting in:  $a_1 = 109.64$  mN m,  $a_2 = 15.56$  N with a  $R^2 = 0.994$  and a  $RMSE = 4.57$  mN m. Perfect compliance is reached for  $d = d_0^{exp} = 6.78$  mm.

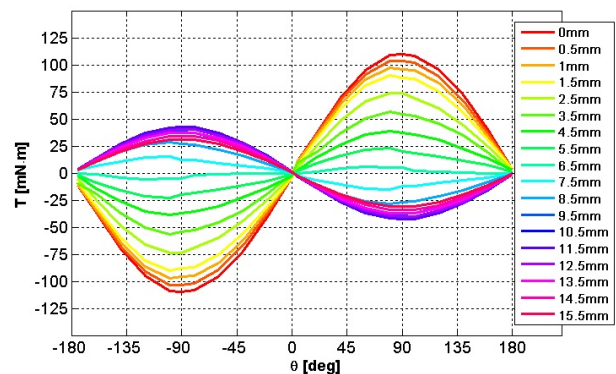


**Figure 8.** Piecewise linear interpolations of torque-angle experimental data for different values of  $d$ . Curves preserve their sinusoidal shape also varying magnet distance  $d$ .

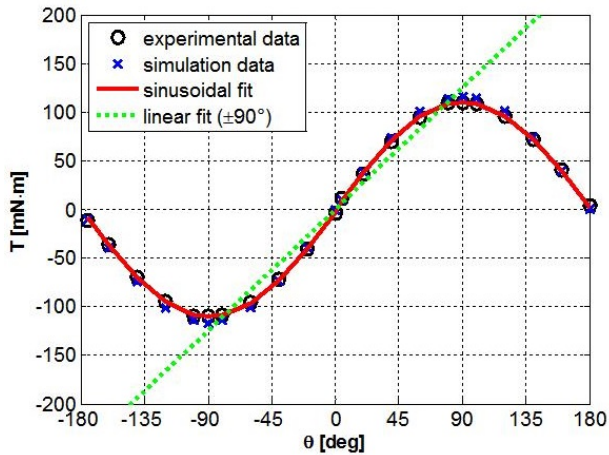


**Figure 9.** Torque-angle profile for  $d = 0$  mm. Experimental data are fitted with  $T(\theta) = b_1 \sin(\theta)$ .  $b_1 = 110.20$  mN.m ( $R^2 = 0.999$ ,  $RMSE = 1.17$  mN.m). Experimental data are fitted also with  $T(\theta) = c_1 \theta$  in the range  $\pm 90^\circ$  obtaining a  $R^2 = 0.920$ , with a  $RMSE = 10.54$  mN.m and a torsion stiffness  $c_1 = 79.41$  mN.m rad $^{-1}$ .

As in the linear regression previously described, this fitting is limited to values of  $d$  within the overlap range ( $0 \text{ mm} \leq d \leq 10 \text{ mm}$ ). When  $A = 102.70$  mN.m and  $B = 12.63$  N, one finds  $RMSE = 1.89$  mN.m and  $R^2 = 0.997$ .

For ( $0 \text{ mm} \leq d \leq 10 \text{ mm}$ ), considering (8), the expected torsion stiffness is:

$$k(\theta, d) = (A - Bd) \cos(\theta) \quad (9)$$

From (9), the maximum stiffness is  $102.70$  mN.m rad $^{-1}$ . The maximum RMS stiffness, in the range  $-90^\circ \leq \theta \leq 90^\circ$ , is  $79.41$  mN.m rad $^{-1}$ . It is possible to notice that (9) is not always positive, i.e., for fixed  $d$ , by increasing (decreasing)  $\theta$  until the torque reaches its maximum (minimum), if  $\theta$  keeps increasing (decreasing), torque decreases (increases). This behaviour is exhibited because the system has two equilibrium positions, one stable at  $\theta = 0^\circ$  and the other one unstable at  $\theta = 180^\circ$ . In a magnetic gearing the possibility to cross an unstable position (i.e., “pole slipping”) may be a desired effect in the case of overloading in order to prevent potential mechanical failures. Of course, such behaviour needs to be carefully taken into account in the design of the system control [46]. With reference to the intended application, let's consider the range  $-90^\circ \leq \theta \leq 90^\circ$ , where stiffness is always positive. The energy stored in the system, considering  $d$  constant, can be derived from (8) as:

$$\int_0^{\theta_0} (A - Bd) \sin(\theta) d\theta = (A - Bd) (1 - \cos(\theta_0)) \quad (10)$$

Considering the maximum rotation ( $\theta_0 = 90^\circ$ ) and  $d = 0$  mm, the energy stored is  $102.70$  mJ. The maximum energy storable in the system is  $203.42$  mJ when  $\theta = 180^\circ$ .

The maximum energy density of MAVERIC and the maximum torque density can be calculated taking into account the volume of the device ( $\frac{\pi}{4} \sum_{i=1}^2 [(D_i^{out})^2 - (D_i^{in})^2] h_i \cong 6.81 \text{ cm}^3$ ), respectively

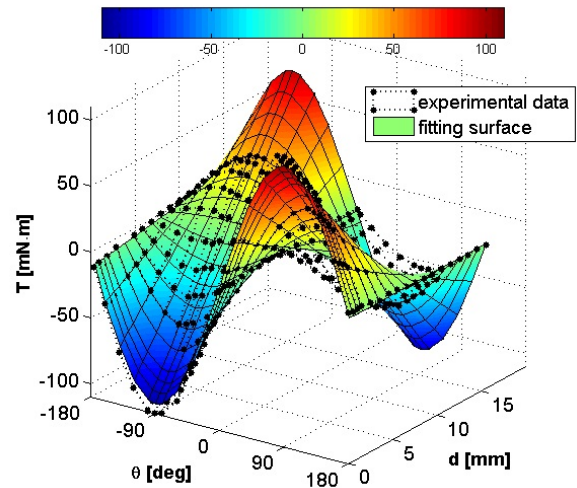


**Figure 10.** Experimental torque values fitted with the surface (8).  $R^2 = 0.997$ ,  $RMSE = 1.89$  mN.m for  $A = 102.70$  mN.m and  $B = 12.63$  N.

obtaining  $29.87 \text{ kJ m}^{-3}$  ( $15.08 \text{ kJ m}^{-3}$  when  $\theta_0$  is  $90^\circ$ ) and  $16.18 \text{ N m}^{-2}$ .

#### 4. Scaling analysis

Magnetostatic FEM simulations, which in Section 3 proved to be reliable and accurate in estimating the mechanical properties of MAVERIC, have also been used to evaluate how geometric dimensions and the number of pole pairs impact the performance of the device in terms of maximum torque, stiffness, torque density and energy density.

In a first set of simulations the number of pole pairs has been taken as the variable parameter ( $N_{pp} = 2 \div 18$ ). The heights of the two magnets have been set to  $10$  mm and the residual induction to  $1455$  mT. The other geometric and magnetic parameters have been given the values in Table 1. For 2, 3, 4 pole pairs, torques have been calculated also varying the relative angular position ( $\theta = 0^\circ \div 90^\circ$  with a step of  $3.75^\circ$ ,  $\theta = 0^\circ \div 60^\circ$  with a step of  $5^\circ$ ,  $\theta = 0^\circ \div 45^\circ$  with a step of  $3.75^\circ$  for  $N_{pp} = 2, 3, 4$ , respectively) and linear position ( $d = 0 \div 15$  mm with a step of  $1$  mm) in order to demonstrate MAVERIC's capability of acting as a disengaged clutch (i.e., perfect compliance) also for  $N_{pp} \neq 1$ . For  $N_{pp} = 2 \div 4$ , torque-angle characteristics ( $d = 0$  mm) are shown in Figure 11, while Figure 12 reports the torque-linear displacement characteristics for  $\theta = 90^\circ / N_{pp}$  (angle which maximizes torque). For all the values of  $N_{pp}$  the maximum torque ( $T_{MAX}$ ) has been computed (13).

In the second set of simulations the number of pole pairs has been kept constant ( $N_{pp} = 1$ ), while geometric parameters have been changed. Overall, 684 geometries have been simulated (Figure 14), considering as variable parameters the radial thicknesses of both the inner and the outer magnets ( $\tau_1 = 5 \div 52.5$  mm,  $\tau_2 = 2.5 \div 52.5$  mm) and their height ( $h_1 = h_2 = H = 2.5 \div 52.5$  mm). For both magnets,  $D_1^{in}$  ( $2$  mm), the residual induction ( $1455$  mT) and the coercive force ( $796 \text{ kA m}^{-1}$ ) have been kept constant. Also the air gap between magnets has

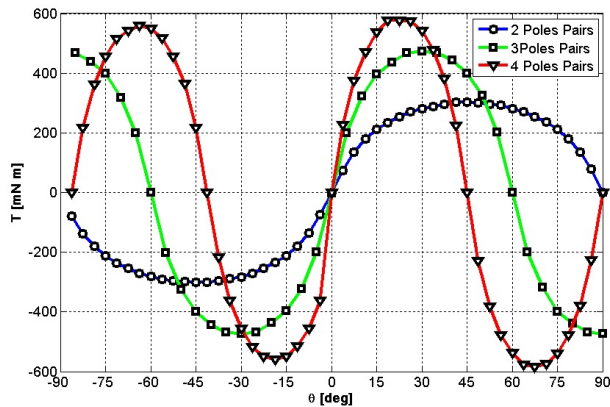


**Figure 11.** Torque angle characteristics ( $d = 0\text{mm}$ ) for 2, 3 and 4 pole pairs and with  $D_1^{\text{out}}, D_2^{\text{out}}, D_1^{\text{in}}, D_2^{\text{in}}$  as in Table 1 and  $h_1 = h_2 = 10\text{mm}$ .

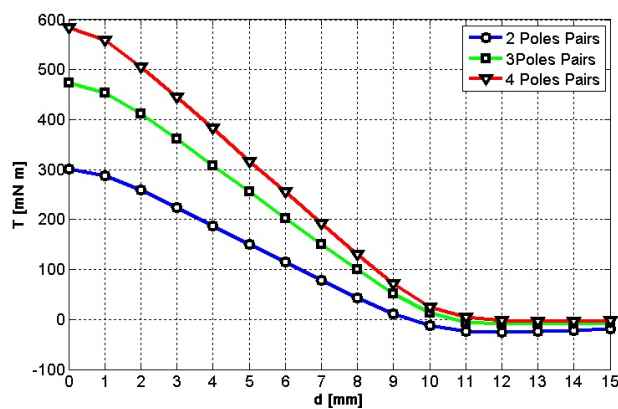


**Figure 12.** Torque-linear displacement characteristics for  $N_{pp} = 2, 3$  and  $4$  with  $\theta$  equal to  $45^\circ, 30^\circ$  and  $22.5^\circ$ .  $D_1^{\text{out}}, D_2^{\text{out}}, D_1^{\text{in}}, D_2^{\text{in}}$  as in Table 1 and  $h_1 = h_2 = 10\text{mm}$ .

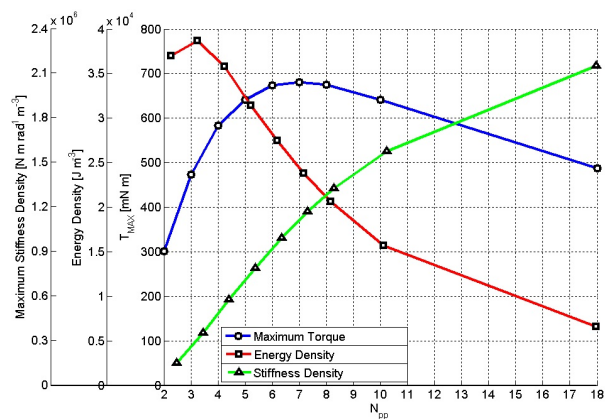


**Figure 13.** Maximum torque  $T_{\text{MAX}}$  (circular markers), energy density (square markers) and maximum stiffness density (triangular markers) computed for  $d = 0\text{mm}$  and  $\theta = 90^\circ / N_{pp}$ , as a function of  $N_{pp}$ .  $D_1^{\text{out}}, D_2^{\text{out}}, D_1^{\text{in}}, D_2^{\text{in}}$  as in Table 1,  $h_1 = h_2 = 10\text{mm}$ .

been kept constant ( $0.5\text{mm}$ ). The geometric bounds have been selected in order to include in the analysis designs which, for their size (i.e., outer diameters in the order of tens of  $\text{mm}$ ) and torques (in the order of tens of  $\text{Nm}$ ), can find practical applications in the fields of biorobotics and wearable robotics.

Properties [unit]	Value	$N_{pp}$
Max. Torque Density [ $\text{N m m}^{-3}$ ]	$166.84 \cdot 10^3$	7
Max. Torque [ $\text{N m}$ ]	0.68	
Max. Energy Density [ $\text{J m}^{-3}$ ]	$38.68 \cdot 10^3$	3
Max. Energy [ $\text{J}$ ]	0.124	
Max. Stiffness [ $\text{N m rad}^{-1}$ ]	8.76	18
Max. Stiffness Density [ $\text{N m rad}^{-1} \text{m}^{-3}$ ]	$2.15 \cdot 10^6$	

**Table 2.** Analysis results of pole pairs ( $\tau_1 = 5\text{mm}$ ,  $\tau_2 = 4.05\text{mm}$ ,  $H = 10\text{mm}$ ).

Properties [unit]	Value	$\tau_1$ [mm]	$\tau_2$ [mm]	H [mm]
Max. Torque Density [ $\text{N m m}^{-3}$ ]	$47.21 \cdot 10^3$	47.5	22.5	32.5
Max. Energy Density [ $\text{J m}^{-3}$ ]				
Max. Stiffness Density [ $\text{N m rad}^{-1} \text{m}^{-3}$ ]	$47.21 \cdot 10^3$	50	52.5	52.5
Max. Energy [ $\text{J}$ ]	70.32			
Max. Torque [ $\text{N m}$ ]	70.32			
Max. Stiffness [ $\text{N m rad}^{-1}$ ]	70.32			

**Table 3.** Geometry scaling analysis results ( $N_{pp} = 1$ ). As it can be verified from (8), (9) and (10), maximum torque, energy and stiffness assume the same numerical value for  $-90^\circ < \theta < 90^\circ$  and  $N_{pp} = 1$  if SI units are used.

#### 4.1. Results

The first set of simulations (constant geometry, variable  $N_{pp}$ ) shows that maximum torque, stiffness and energy increase with  $N_{pp}$  (Figure 13). In particular, for the geometry described in Section 4, the maximum torque density is  $166.84 \cdot 10^3 \text{N m m}^{-3}$  for  $N_{pp} = 7$ , the maximum energy density is  $38.68 \cdot 10^3 \text{J m}^{-3}$  for  $N_{pp} = 3$  and the maximum stiffness density is  $2.15 \cdot 10^6 \text{N m rad}^{-1}$  for  $N_{pp} = 18$  (Table 2).

The second set of simulations (variable geometry,  $N_{pp} = 1$ ) allowed us to identify the geometries that maximize torque, stiffness and energy per unit volume. It is to be noted that, in the case under consideration ( $N_{pp} = 1$ ), the latter two values numerically coincide for each geometry.

In detail, simulations returned a maximum energy density of  $47.21 \cdot 10^3 \text{J m}^{-3}$  and a maximum torque density of  $47.21 \cdot 10^3 \text{N m m}^{-3}$  for  $\tau_1 = 47.5\text{mm}$ ,  $\tau_2 = 22.5\text{mm}$ ,  $H = 32.5\text{mm}$  (Figure 15) and a maximum torque of  $70.32 \text{N m}$  in correspondence to upper bounds ( $\tau_1 = 50\text{mm}$ ,  $\tau_2 = 52.5\text{mm}$ ,  $H = 52.5\text{mm}$ ), as summarized in Table 3.

#### 5. Example applications

The scaling analysis reported above can be used to adapt the design of MAVERIC to specific needs. One example



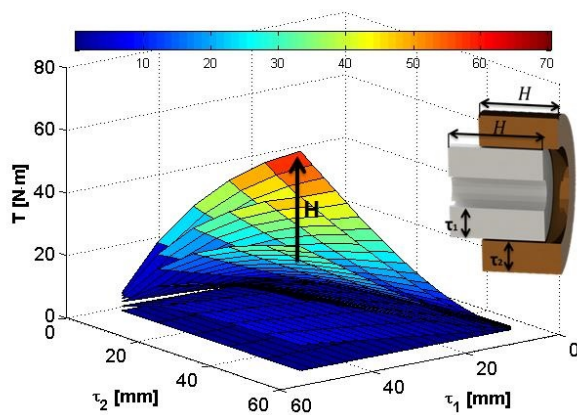


**Figure 14.** Maximum torque as a function of magnet dimensions. Height of magnet ( $H$ ) varies from 2.5 mm to 52.5 mm by steps of 10 mm. Maximum torque increases with dimensions. When  $\tau_1 = 50$  mm,  $\tau_2 = 52.5$  mm,  $H = 52.5$  mm the maximum torque is 70.32 Nm.

Properties [unit]	Value
Max. Torque [N m]	55.52
Stiffness [N m rad <sup>-1</sup> ]	0 ÷ 388.64
Torque Density [N m m <sup>-3</sup> ]	$852.58 \cdot 10^3$
Energy Density [J m <sup>-3</sup> ]	$121.77 \cdot 10^3$
Energy [J]	7.93
Stiffness Density [N m rad <sup>-1</sup> m <sup>-3</sup> ]	$5.97 \cdot 10^6$
Perfect Compliance Distance [mm]	33.3

**Table 4.** Calculated performance for  $N_{pp} = 7$ ,  $\tau_1 = 36$  mm,  $\tau_2 = 20$  mm,  $H = 20$  mm.

application is in the field of resonant motors for biorobotic applications [48]. In nature several animal species generate oscillatory movements by exploiting body stiffness, and this principle can be replicated in robots by properly coupling a motor to a compliant element acting as a spring. For example, the device presented in [48] uses a torsion spring with a stiffness of  $1.6 \cdot 10^{-3}$  N m rad<sup>-1</sup> and a stiffness density, calculated from the data reported in the paper of about  $2.32 \cdot 10^4$  N m rad<sup>-1</sup> m<sup>-3</sup>. Both values can be rendered by MAVERIC, as shown in the previous section. Moreover, a variable stiffness compliant element would allow us to efficiently tune the oscillation frequency without compromising efficiency. As already mentioned, another important class of potential applications is represented by VIAs and SEAs. For example, let's set as design targets a minimum peak torque  $T_{em} \cong 60$  N m, a stiffness of about 300 N m rad<sup>-1</sup>, a deflection angle  $\theta_{max} = 10^\circ \div 15^\circ$ , a maximum diameter of 120 mm and a thickness of 20 mm. Considering the state of the art, such a spring would fit compliant actuators with a nominal power in the range 300 – 600 W [25–27]. For such a design, the number of pole pairs needed is approximately given by  $N_{pp} = 90^\circ / \theta_{max}$ . Let's set  $N_{pp} = 7$  (rounding to the closest lower integer of  $90^\circ / 12.5^\circ$ ). A preliminary design can be obtained by considering the scaling analysis results related to the case  $N_{pp} = 1$ . The torque is almost directly proportional to the

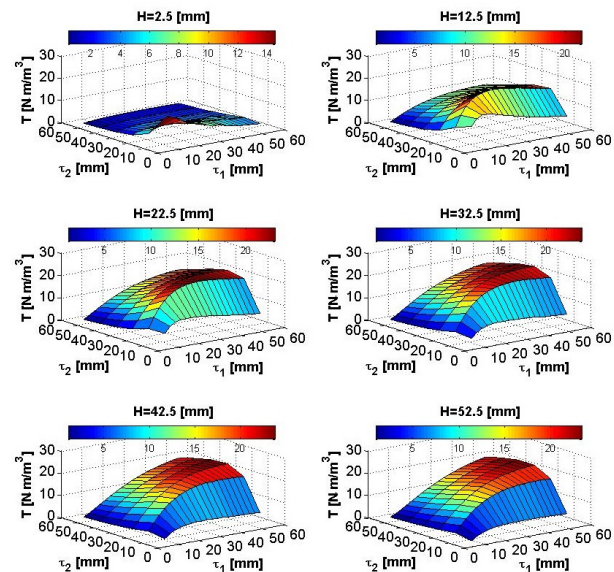


**Figure 15.** Torque density for different geometries. Maximum torque density is  $23.82$  N m m<sup>-3</sup> for  $\tau_1 = 47.5$  mm,  $\tau_2 = 22.5$  mm and  $H = 32.5$  mm.

number of pole pairs. For a given geometry, if  $T_1$  is the maximum torque when  $N_{pp} = 1$ , then the actual torque is approximately given by  $N_{pp} T_1$ . The geometry, which for  $N_{pp} = 1$  provides an expected torque not less than  $T_{em} / N_{pp}$ , is characterized by the following geometric parameters:  $\tau_1 = 30$  mm,  $\tau_2 = 22.5$  mm,  $H = 22.5$  mm. In fact, a device with such dimensions expectedly provides a maximum torque of  $8.75$  N m  $> 8.57$  N m =  $T_{em} / N_{pp}$ . In order to comply with the design requirement on height, this geometry needs to be slightly adapted as follows:  $\tau_1 = 36$  mm,  $\tau_2 = 20$  mm,  $H = 20$  mm. Numerical simulations are necessary to refine the evaluation of the expected performance. Simulations retrieved a maximum torque (for  $\theta = 90^\circ / N_{pp}$ ) of  $T_{MAX} = 55.52$  N m, a maximum stiffness of  $388.64$  N m rad<sup>-1</sup> and a maximum stored energy of 7.93 J (Table 4), in line with the design targets. For this device, the distance between the magnets at which perfect compliance occurs is  $d_0 = 33.3$  mm, as it can be retrieved by linearly interpolating the torques for  $\theta = 90^\circ / 7$  when  $d$  varies from 0 mm to 42 mm with a step of 2 mm. Overall, the outer diameter of the spring is 115 mm, while the thickness varies from 20 mm to 55.3 mm, depending on the value of  $d$ .

The two examples reported above show how the MAVERIC principle can be applied in robotics. The potential drawback represented by dimensions and weight in certain applications may be counterbalanced by a number of positive aspects. First of all MAVERIC is not affected by overloading issues, because an excessive torque would cause pole slipping, thus preventing mechanical failures, which may conversely occur in metal springs [27]. Moreover, MAVERIC intrinsically has an infinite fatigue life. While the two above-mentioned advantages are characteristic of magnetic couplers, MAVERIC is characterized by a third feature, consisting of its capability to continuously vary the intrinsic stiffness from a maximum value down to the perfect compliance condition. Once set, stiffness can be kept constant without



supplying current, e.g., by using a non-backdriveable mechanism to adjust  $d$ , with energetic advantages over existing solutions (e.g., [20]). Variable intrinsic stiffness is important, for example, to efficiently modulate the frequency of resonant motors, to tune the stiffness of compliant actuators or to separate the load from the actuator without resorting to control-based strategies or additional mechanical components (e.g., clutches).

## 6. Conclusions and future work

In this paper we reported on a novel concept of a magnetic variable stiffness coupler that can also be used as a clutch. Both simulations and experimental measurements have been performed to prove the effectiveness of the proposed concept. The proposed device offers a good trade-off between compactness, reliability, variable compliance and backdrivability. Scaling analysis indicates a maximum torque density of  $166.84 \cdot 10^3 \text{ N m m}^{-3}$ . Simulations show that a large range of stiffness, maximum stored energy and torque can be obtained by changing dimensions and the number of pole pairs. Therefore, the actual embodiment of the MAVERIC principle can be chosen in order to meet the requirements of specific applications. To this end, a semi-analytical model, inspired by [47], will be implemented in order to obtain a computationally efficient tool for optimizing MAVERIC for specific applications. Furthermore, a VSA incorporating a MAVERIC is under development for the actuation of the spine of a robotic fish [49].

## 7. References

- [1] Kim BS, Song JB (2012) Design and Control of a Variable Stiffness Actuator Based on Adjustable Moment Arm. *IEEE Trans. Robot.* 28:1145-1151.
- [2] Mouri T, Kawasaki H, Koketsu K (2011) Compact torque sensor for a robot hand. In: *International Conference on Ubiquitous Robots and Ambient Intelligence (URAI)*. 2011 Nov 23-26; Incheon, Korea. pp. 439-441.
- [3] Tsetserukou D, Tadakuma R, Kajimoto H, et al. (2006) Optical torque sensors for implementation of local impedance control of the arm of humanoid robot. In: *2006 IEEE International Conference on Robotics and Automation (ICRA)*. 2006 May 15-19; Orlando, USA. pp. 1674-1679.
- [4] Finio BM, Galloway KC, Wood RJ (2011) An ultra-high precision, high bandwidth torque sensor for microrobotics applications. In: *2011 IEEE/RSJ International Conference on Intelligent Robots and Systems (IROS)*. 2011 Sep 25-30; San Francisco, USA. pp. 31-38.
- [5] Liljebäck P, Stavdahl O, Pettersen KY, et al. (2012) A modular and waterproof snake robot joint mechanism with a novel force/torque sensor. In: *IEEE/RSJ International Conference on Intelligent Robots and Systems (IROS)*. 2012 Oct 7-12; Vilamoura, Portugal. pp. 4898-4905.
- [6] Pratt G, Williamson M (1995) Series elastic actuators. In: *1995 IEEE/RSJ International Conference on Intelligent Robots and Systems 95 'Human Robot Interaction and Cooperative Robots'*. 1995 Aug 5-9; Pittsburgh, PA, USA. pp. 399-406.
- [7] Carpino G, Accoto D, Sergi F, et al. (2012) A novel compact torsional spring for series elastic actuators for assistive wearable robots. *J. Mech. Des.* 134:121002.
- [8] Sergi F, Accoto D, Carpino G, et al. (2012) Design and characterization of a compact rotary series elastic actuator for knee assistance during overground walking. In: *IEEE RAS EMBS International Conference on Biomedical Robotics and Biomechatronics (BioRob)*. 2012 Jun 24-27; Rome, Italy. pp. 1931-1936.
- [9] Accoto A, Carpino G, Sergi F, et al. (2013) Design and characterization of a novel high-power series elastic actuator for a lower limb robotic orthosis. *Int. j. adv. robot. syst.* DOI:10.5772/56927
- [10] Tonietti G, Schiavi R, Bicchi A (2005) Design and Control of a Variable Stiffness Actuator for Safe and Fast Physical Human/Robot Interaction. In: *IEEE International Conference on Robotics and Automation (ICRA)*. 2005 Apr 18-22; Barcelona, Spain. pp. 526-531.
- [11] Tagliamonte NL, Sergi F, Carpino G, et al. (2010) Design of a variable impedance differential actuator for wearable robotics applications. In: *2010 IEEE/RSJ International Conference on Intelligent Robots and Systems (IROS)*. 2010 Oct 18-22; Taipei, Taiwan. pp. 2639-2644.
- [12] Kim BS, Park JJ, Song JB (2007) Double Actuator Unit with Planetary Gear Train for a Safe Manipulator. In: *IEEE International Conference on Robotics and Automation (ICRA)*. 2009 May 12-17; Kobe, Japan. pp. 1146-1151.
- [13] Choi J, Hong S, Woosub L, et al. (2009) A variable stiffness joint using leaf springs for robot manipulators. In: *IEEE International Conference on Robotics and Automation (ICRA)*. 2009 May 12-17; Kobe, Japan. pp. 4363-4368.
- [14] Schiavi R, Grioli G, Sen S, et al. (2008) VSA-II: a novel prototype of variable stiffness actuator for safe and performing robots interacting with humans. In: *IEEE International Conference on Robotics and Automation (ICRA)*. 2008 May 19-23; Pasadena, CA, USA. pp. 2171-2176.
- [15] Wolf S and Hirzinger G (2008) A new variable stiffness design: Matching requirements of the next robot generation. In: *IEEE International Conference on Robotics and Automation (ICRA)*. 2008 May 19-23; Pasadena, CA, USA. pp. 1741-1746.
- [16] Hurst JW, Chestnutt JE, Rizzi AA (2004) An actuator with physically variable stiffness for highly dynamic legged locomotion. In: *IEEE International Conference on Robotics and Automation (ICRA)*. 2004 Apr 26-May 1; New Orleans, USA. pp. 4662-4667.
- [17] Jafari A, Tsagarakis NG, Caldwell DG (2013) A Novel Intrinsically Energy Efficient Actuator With Adjustable Stiffness (AwAS). *IEEE-ASME Trans. Mechatron.* 18:355-365.
- [18] Groothuis SS, Rusticelli G, Zucchelli A, et al. (2012) The vsaUT-II: A novel rotational variable stiffness

- actuator. In: 2012 IEEE International Conference on Robotics and Automation (ICRA). 2012 May 14-18; Saint Paul, MN, USA. pp. 3355-3360.
- [19] Van Ham R, Sugar T, Vanderborght B, et al. (2009) Compliant actuator designs. *IEEE Rob. Autom Mag.* 16:81-94.
  - [20] Fasse ED, Hogan N, Gomez SR et al. (1994) A novel variable mechanical impedance electromechanical actuator. In: *Dynamic Systems and Control Conference (DSCC)*. 1994; 55:311-318.
  - [21] Tagliamonte NL, Sergi F, Accoto D, et al. (2012) Double actuation architectures for rendering variable impedance in compliant robots: A review. *Mechatronics*. 22:1187-1203.
  - [22] Sensinger J, Weir R (2008) User-modulated impedance control of a prosthetic elbow in unconstrained, perturbed motion. *IEEE Trans. Biomed. Eng.* 55:1043-1055.
  - [23] Tsagarakis N, Laffranchi M, Vanderborght B, et al. (2009) A compact soft actuator unit for small scale human friendly robots. In: *IEEE International Conference on Robotics and Automation (ICRA)*. 2009 May 12-17; Kobe, Japan. pp. 4356-4362.
  - [24] Wyeth G (2008) Demonstrating the safety and performance of a velocity sourced series elastic actuator. In: *IEEE International Conference on Robotics and Automation (ICRA)*. 2008 May 19-23; Pasadena, CA, USA. pp. 3642-3647.
  - [25] Veneman JF, Ekkelenkamp R, Kruidhof R, et al. (2006) A series elastic-and bowden-cable-based actuation system for use as torque actuator in exoskeleton-type robots. *Int. J. Robot. Res.* 25:261-281.
  - [26] Stienen AHA, Hekman EEG, Braak H, et al. (2010) Design of a Rotational Hydroelastic Actuator for a Powered Exoskeleton for Upper Limb Rehabilitation. *IEEE Trans. Biomed. Eng.* 57:728-735.
  - [27] Lagoda C, Schouten A, Stienen A, et al. (2010) Design of an electric series elastic actuated joint for robotic gait rehabilitation training. In: *IEEE RAS and EMBS International Conference on Biomedical Robotics and Biomechatronics (BioRob)*. 2010 Sep 26-29; Tokyo, Japan. pp. 21-26.
  - [28] Accoto D, Tagliamonte NL, Carpino G, et al. (2012) pVEJ: A novel modular passive viscoelastic joint for wearable robots. In: *2012 IEEE International Conference on Robotics and Automation (ICRA)*. 2012 May 14-18; Saint Paul, MN, USA. pp. 3361-3366.
  - [29] Sergi F, Accoto D, Tagliamonte NL, et al. (2011) A systematic graph-based method for the kinematic synthesis of non-anthropomorphic wearable robots for the lower limbs. *Front. Mech. Eng.* 6:61-70.
  - [30] Veneman JF, Ekkelenkamp R, Kruidhof R, et al. (2005) Design of a series elastic- and Bowden cable-based actuation system for use as torque-actuator in exoskeleton-type training. In: *IEEE International Conference on Rehabilitation Robotics*. 2005 Jun 28-Jul 1; Chicago, Illinois, USA. pp. 496-499
  - [31] Campbell E, Kong Z, Hered W, et al. (2011) Design of a low-cost series elastic actuator for multi-robot manipulation. In: *IEEE International Conference on Robotics and Automation (ICRA)*. 2011 May 9-13; Shanghai, China. pp. 5395-5400.
  - [32] Kong K, Bae J, Tomizuka M (2011) A compact rotary series elastic actuator for human assistive systems. *IEEE/ASME Trans. Mechatron.* 17:288-297.
  - [33] Ragonesi D, Agrawal S, Sample W, et al. (2011) Series elastic actuator control of a powered exoskeleton. In: *2011 Annual International Conference of the IEEE Engineering in Medicine and Biology Society (EMBC)*. 2011 Aug 30-Sep 3; Boston, MA, USA. pp. 3515-3518.
  - [34] Legault MA, Lavoie MA, Cabana F, et al. (2008) Admittance control of a human centered 3 DOF robotic arm using differential elastic actuators. In: *2010 IEEE/RSJ International Conference on Intelligent Robots and Systems (IROS)*. 2008 Sep 22-26; Nice, France. pp. 4143-4144.
  - [35] Simi M, Gerboni G, Menciassi A, et al. (2013) Magnetic torsion spring mechanism for a wireless biopsy capsule. *J. Med. Devices*. doi:10.1115/1.4025185.
  - [36] Montague R, Bingham C, Atallah K (2012) Servo Control of Magnetic Gears. *IEEE/ASME Trans. Mechatron.* 17:269-278.
  - [37] Faisal ARM, Hong C, Chung GS (2012) Multi-frequency electromagnetic energy harvester using a magnetic spring cantilever. *Sens. Actuator A-Phys.* 182:106-113.
  - [38] Robertson W, Cazzolato B, Zander A. (2005) A multipole array magnetic spring. *IEEE Trans. Magn.* 41:3826-3828.
  - [39] Qian KX, Zeng P, Ru WM, et al. (2003) Novel magnetic spring and magnetic bearing. *IEEE Trans. Magn.* 39:559-561.
  - [40] Faisal AR, Chung G S (2012) Design and Analysis of a Vibration-driven AA Size Electromagnetic Energy Harvester Using Magnetic Spring. *IEEE Trans. Electr. Electron. Eng.* 13:125-128
  - [41] Headstrom P (2011) Magnetic spring system in a resonant motor. European Patent EP 2375098; issued 2011 Oct 12.
  - [42] Park S (2008) Design of a robot joint with variable stiffness. In: *IEEE International Conference on Robotics and Automation (ICRA)*. 2008 May 19-23; Pasadena, CA, USA. pp. 1760-1765.
  - [43] Ravaut R, Lemarquand G (2010) Synthesis about Analytical Approaches for Calculating the Magnetic Field Produced by Permanent Magnets of Various Topologies. In: *Progress In Electromagnetics Research Symposium Proceedings*. 2010 Jul 5-8; Cambridge, USA. pp. 154-158.
  - [44] Coey JMD (2010) Magnetism and magnetic materials. Dublin: Cambridge University Press. 28.
  - [45] Gieras JF, Wing M (2002) Permanent magnet motor technology: design and applications New York: Marcel Dekker. 103.
  - [46] Montague R G, Bingham C, Atallah K (2012) Magnetic Gear Pole-Slip Prevention Using Explicit Model Predictive Control. *IEEE/ASME Trans. Mechatron.* 99:1-9.

- [47] Furlani EP, Wang R, Kusanadi H (1995) A three-dimensional model for computing the torque of radial couplings. *IEEE Trans. Magn.* 31:2522-2526.
- [48] Campolo D, Azhar M, Lau G, et al. (2012) Can DC motors directly drive flapping wings at high frequency and large wing strokes?. *IEEE/ASME Trans. Mechatron.* 99:1-12.
- [49] Alessi A, Sudano A, Accoto D, et al. (2012) Development of an autonomous robotic fish. In: *IEEE RAS EMBS International Conference on Biomedical Robotics and Biomechatronics (BioRob)*. 2012 Jun 24-27; Rome, Italy. pp. 1032-1037.